Supporting information

3D printing flexible zinc-ion microbatteries with ultrahigh areal capacity and energy density for wearable electronic

Weibin Yan,†[a] Xinze Cai,†[a] Feipeng Tan,[a] Jiahui Liang,[a] Jiangqi Zhao*[ac] and Chaoliang Tan*[b]

a. College of Materials Science and Engineering, Sichuan University, Chengdu 610065, China. E-mail: Jiangqizhao@scu.edu.cn

b. Department of Chemistry and Center of Super-Diamond and Advanced Films (COSDAF), City University of Hong Kong, Kowloon, Hong Kong SAR 999077, China. E-mail: chaoltan@cityu.edu.hk

c. Engineering Research Center of Alternative Energy Materials and Devices, Ministry of Education, Chengdu 610065, China.

† W. Yan and X. Cai contributed equally to this work.

Experiment section

Chemicals

Vanadium pentoxide (V_2O_5, AR, 99.0%), cerium chloride heptahydrate ($CeCl_3 \cdot 7H_2O$, AR, 99.0%), H_2O_2 (AR, 30.0%), HF (AR, 30.0%), zinc trifluoromethane sulfonate ($Zn(CF_3SO_3)_2$, AR, 98%), carboxylic carbon nanotube (CNT, 98%), N-methyl-2-pyrrolidone (NMP, AR, 99%) and poly-(vinylidene fluoride) (PVDF) were purchased from Aladdin. All chemicals are used directly without further treatment.

Preparation of Ce doped V_2O_5 (CVO) and F/Ce co-doped V_2O_5 (FCVO)

0.3 g V_2O_5 was dissolved in 50 mL deionized water by stirring continuously for 0.5 h in a water bath at 50 ℃, followed by the addition of 4 mL H_2O_2 under continuous stirring for another 0.5 h . When the solution turned a clear orange, 0.04 g $CeCl_3 \cdot 7H_2O$ was added into above solution and magnetically stirred until a homogeneous solution was formed. Then the solution was quickly transferred into a 50 mL Teflon-lined sealed autoclave, and maintained at 180 ℃ for 24 h in the oven. The product was collected and washed with deionized water and ethanol for 3 times, and the CVO were obtained after drying at 60 ℃ for 12 hours at the oven.

The FCVO was obtained by adding 5 μL HF into the $V_2O_5/CeCl_3 \cdot 7H_2O$ mixed solution before transferring into Teflon-lined sealed autoclave, and the other operation steps remained the same as that of CVO.

Preparation of printing inks

A fluid cathode ink was prepared by dispersing 50 mg FCVO, 10 mg carbon black (CB), 30 mg CNT, and 10 mg PVDF in 400 mg NMP by stirring for 30 min to obtain an evenly mixed ink (FCVO/CB/CNT). To research the influence of CNT, the FCVO/CB ink was prepared by dispersing 50 mg FCVO, 40 mg CB, and 10 mg PVDF in 400 mg NMP. Furthermore, the preparation formula of anode ink was the same as that of the FCVO/CB/CNT ink, except that FCVO was replaced by Zn powder.

Preparation of gel electrolyte

2 g PVA was added into 20 ml 3 M $Zn(CF_3SO_3)_2$ solution, followed by vigorous stirring at 95 °C until the solution turned clear. The $Zn(CF_3SO_3)_2$/PVA gel electrolyte was obtained when it returned to room temperature.

3D Printing of ZIMBs

First, the as-prepared cathode ink was transferred into a syringe, and extruded onto the ultra-thin polyethylene terephthalate (PET) substrate (the thickness of PET is 0.025 mm and the size of PET is 3×7 cm) at a rate of 17 mg/s. Subsequently, the anode ink was printed on the PET substrate with similar way. After fully dry of the printed electrodes at 60 °C, 5 ml $Zn(CF_3SO_3)_2$/PVA gel electrolyte was extruded into the interspace between adjacent microelectrodes to obtain the flexible ZIMBs.

Materials characterization

The morphologies of the samples were observed by scanning electron microscopy (SEM, Hitachi Regulus8100, Japan) and high-resolution transmission electron microscopy (HRTEM, FEI Tecnai F20). The structures of the samples were studied by X-ray diffraction (XRD, Rigaku Ultima IV, Japan) with Cu Kα radiation at a scanning rate of 2 °/min, Raman spectroscopy (Horiba LabRAM HR Evolution, Japan) and X-ray photoelectron spectroscopy (XPS, Thermo Scientific K-Alpha, America)

Electrochemical measurements

Cyclic voltammograms (CV) and electrochemical impedance spectra (EIS) were investigated on an electrochemical workstation (CHI760). Galvanostatic charge/discharge (GCD) and galvanostatic intermittent titration technique (GITT) were performed at NEWARE battery tests. The gravimetric capacity density (C_g) and gravimetric energy density (E_g) can be read directly from the NEWARE software. Moreover, the other properties can be calculated using the following formulas:[S1,S2]

$$C_a = M_a \times C_g \quad (1)$$

$$E_a = M_a \times E_g \quad (2)$$

$$P_a = \frac{E_a}{\Delta t} \tag{3}$$

where C_a is the areal capacity density; M_a is the areal mass loading; E_a is the areal energy density; P_a is the areal power density; Δt is the discharge time.

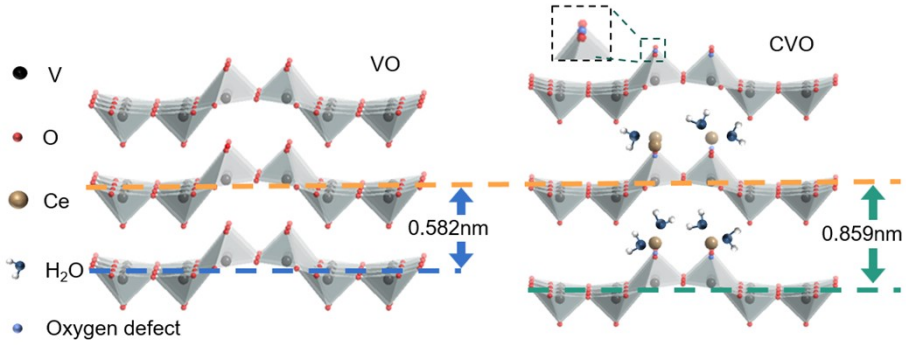

Fig. S1 Schematic of the VO and CVO crystal structure.

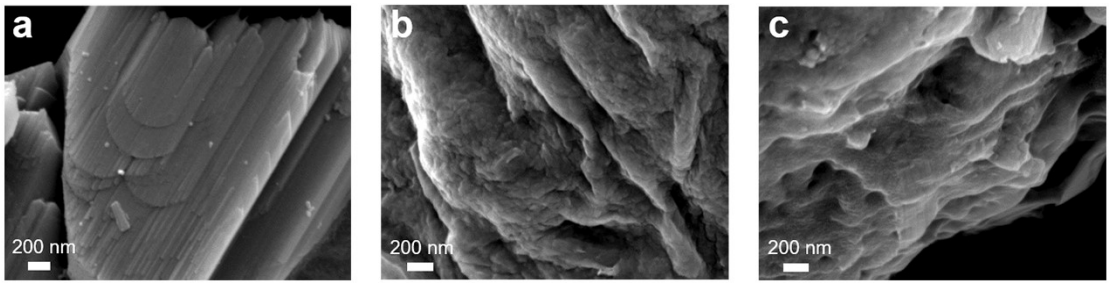

Fig. S2 SEM images of (a) VO, (b) CVO and (c) FCVO.

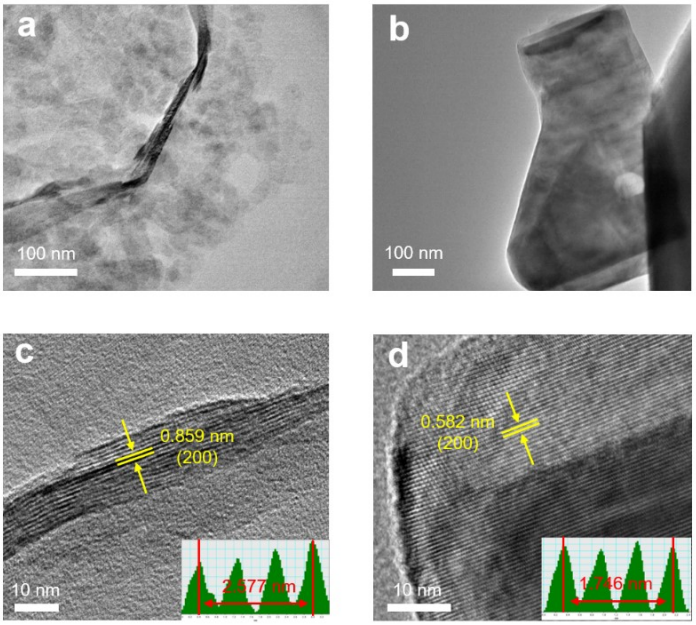

Fig. S3 TEM images of (a) CVO and (b) VO. HRTEM images of (c) CVO and (d) VO (inset: the corresponding line-scan of HRTEM intensity analysis).

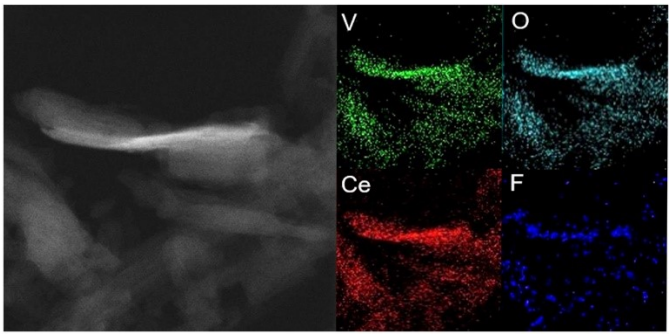

Fig. S4 EDX element mapping images of FCVO.

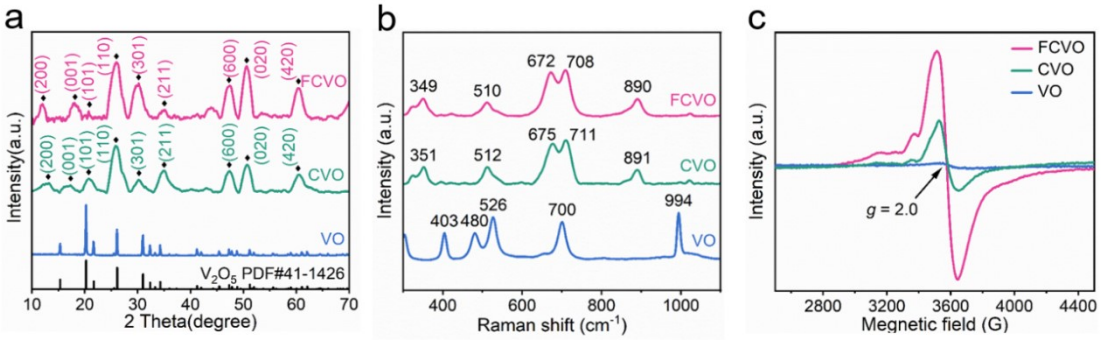

Fig. S5 (a) XRD patterns, (b) Raman spectra and (c) EPR spectra of VO, CVO and FCVO.

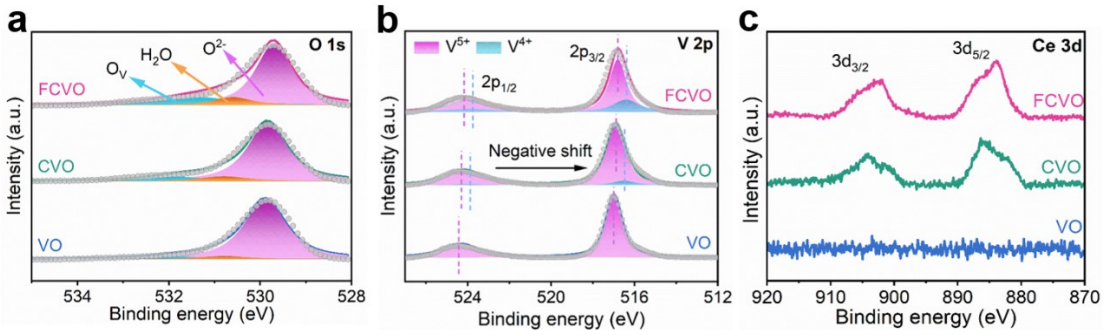

Fig. S6 (a) O 1s, (b) V 2p and (c) Ce 3d spectra of VO, CVO and FCVO.

XPS was conducted to analyze the chemical compositions and the valence states of the samples. As shown in Fig. S6a, the characteristic peaks at around 531.4 eV, 530.7 eV and 529.8 eV correspond to oxygen-deficient, V-OH and V-O-V, respectively.[S3,S4] The obvious enhancement of the peak intensity at 531.4 eV confirms the enrichment of oxygen defects for FCVO. Fig. S6b displays the V 2p XPS spectrum with two peaks at 524.4 and 516.9 eV, which can be further deconvoluted to more peaks corresponding to V^{5+} (red) and V^{4+} (blue). Compared with that of VO, the peaks for FCVO display negative shift and the intensity of V^{4+} become higher, reflecting that fewer O neighbors around V on average.[S5] Different with that of VO, the high-resolution XPS spectra of Ce 3d for CVO and FCVO displays two main peaks at 904.0 and 885.9 eV (Fig. S6c), corresponding to $3d_{5/2}$ and $3d_{3/2}$, respectively. The above results indicate the successful co-doping of Ce and F in FCVO, which not only widen the layer spacing of VO, but also induce abundant oxygen defects. This is expected to effectively improve the electrochemical performance of VO.

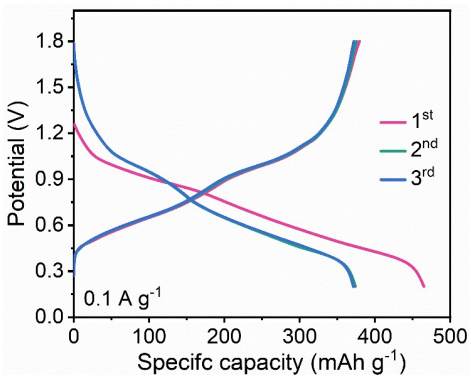

Fig. S7 GCD profiles of FCVO in the initial 3 cycles.

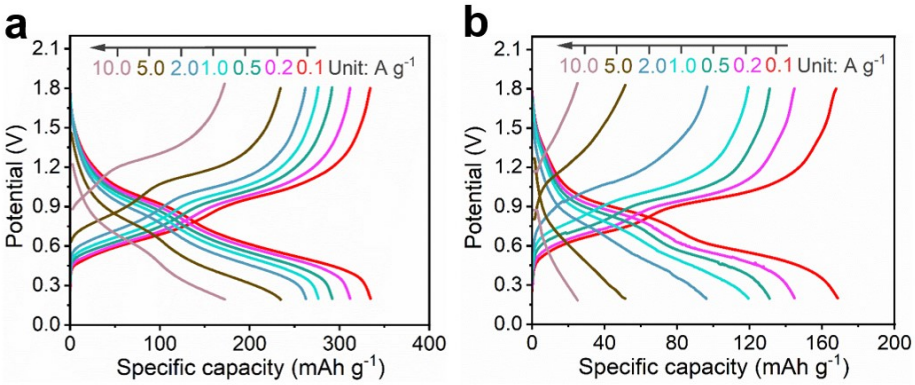

Fig. S8 GCD profiles of (a) CVO and (b) VO at various current densities.

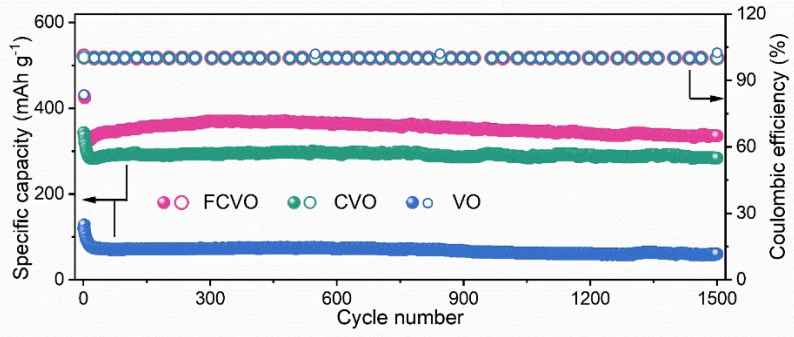

Fig. S9 Long-term cycling stability of VO, CVO and FCVO at 5 A g^{-1}.

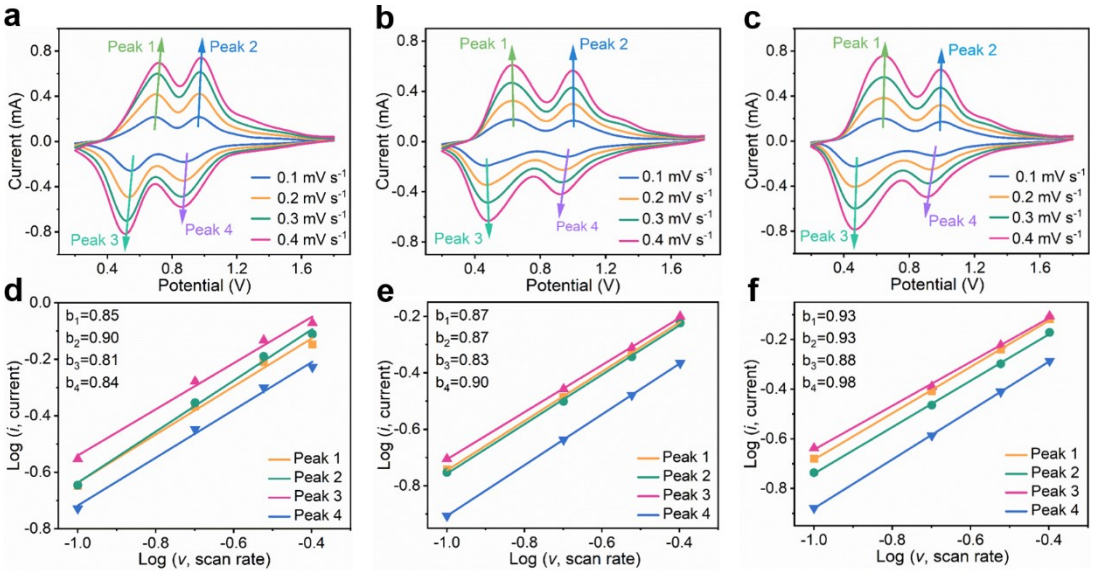

Fig. S10 CV profiles of (a) VO, (b) CVO and (c) FCVO at different scan rates. The fitting lines between log(i) and log(v) at specific peak currents from CV curves: (d) VO, (e) CVO and (f) FCVO.

CV measurements of these samples at different scan rates (0.1−0.4 mV s^{-1}) were conducted to further study their reaction kinetics (Fig. S10a-c). As the scan rate increases, the CV curves show similar shapes, with the redox peaks becoming large gradually. The relationship between the peak current (i) and scan rate (v) obeys the power law ($i = av^b$, where a and b are adjustable parameters).[S6] The value of b is in the range 0.5−1.0, and when b = 0.5 indicates the diffusion control, while b = 1.0 presents the capacitive effect.[S6] For FCVO, the calculated b values of peaks 1, 2, 3, and 4 are 0.93, 0.93, 0.88 and 0.98, respectively (Fig. S10d), which are much higher than that of CVO (Fig. S10e) and VO (Fig. S10f), suggesting a favored capacitive kinetics in FCVO.[S7]

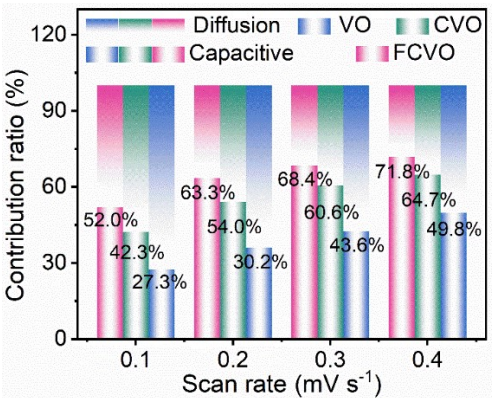

Fig. S11 Diffusion and capacitive contribution of VO, CVO and FCVO at different scan rates.

Based on Fig. S10, the percentages of capacitive contributions of FCVO are 52.0%, 63.3%, 68.4%, and 72.8% at scan rates of 0.1, 0.2, 0.3, and 0.4 mV s^{-1}, respectively, demonstrating that the capacitive effect plays a leading role in the kinetics reaction (Fig. S11). Moreover, the percentages of capacitive contributions of FCVO are higher than those of CVO and VO for all scan rates, which indicates that the co-doping of Ce and F improves the electrochemical reaction kinetics of FCVO.[S8,S9]

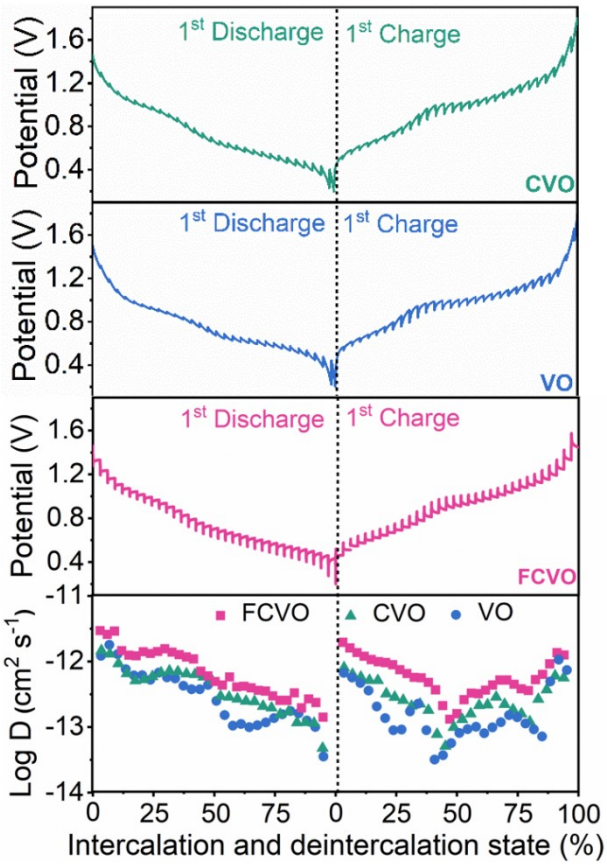

Fig. S12 GITT profiles for VO, CVO and FCVO and the corresponding ion diffusion coefficients .

The GITT was conducted to analyze the ion diffusion coefficient (*D*) in cathodes. the *D* values of FCVO are in the range of 10^{-13}–10^{-11} cm^2 s^{-1}, which are 10−100 times higher than those of CVO (10^{-13}–10^{-12} cm^2 s^{-1}) and VO (10^{-14}–10^{-12} cm^2 s^{-1}), proving that the co-doping of Ce and F is beneficial to enhancing the ion diffusion in VO.[S10,S11]

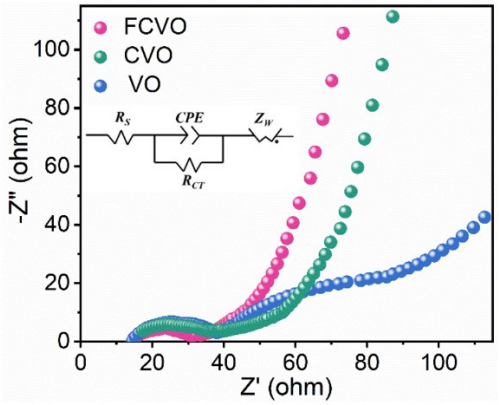

Fig. S13 EIS curves of VO, CVO and FCVO.

Table S1 Fitting results of R_s and R_{ct} of the EIS in Figure S13.

Sample	R_s (Ω)	R_{ct} (Ω)
VO	14.4	26.0
CVO	14.2	24.5
FCVO	13.5	19.4

Note: R_s is the series resistance of the electrochemical system; R_{ct} is the charge-transfer resistance.

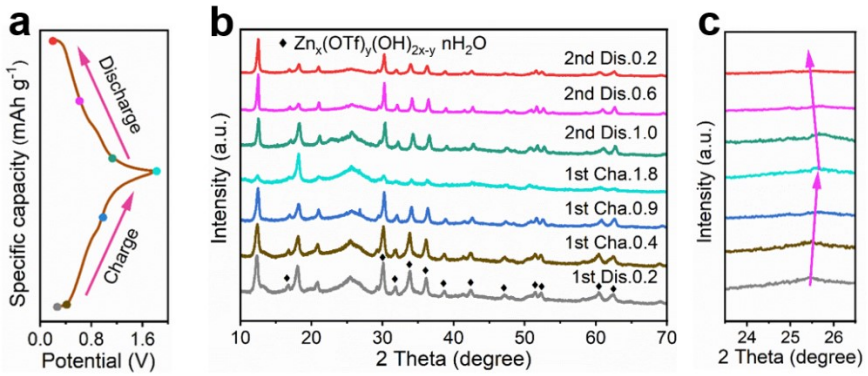

Fig. S14 (a) Charge/discharge curve of FCVO at 0.1 A g^{-1}. (b) Ex situ XRD patterns and (c) the corresponding magnified XRD patterns for the FCVO electrode.

It is worth noting that some peaks of new phase signed in Fig. S14b raised when discharge to 0.2 V, corresponding to the characteristic peaks of $Zn_x(OTf)_y(OH)_{2x-y}\cdot nH_2O$.[S12,S13] During the charging process, these peaks gradually disappear, indicating the great reversibility of chemical reactions. Moreover, in the magnified XRD images (Fig. S14c), the peak located around 25.5° shifts toward lower values slightly during discharge process, and then recovers to the original state during the charging process, which is due to the expansion and contraction of the lattice distance caused by ion intercalation and deintercalation.[S14]

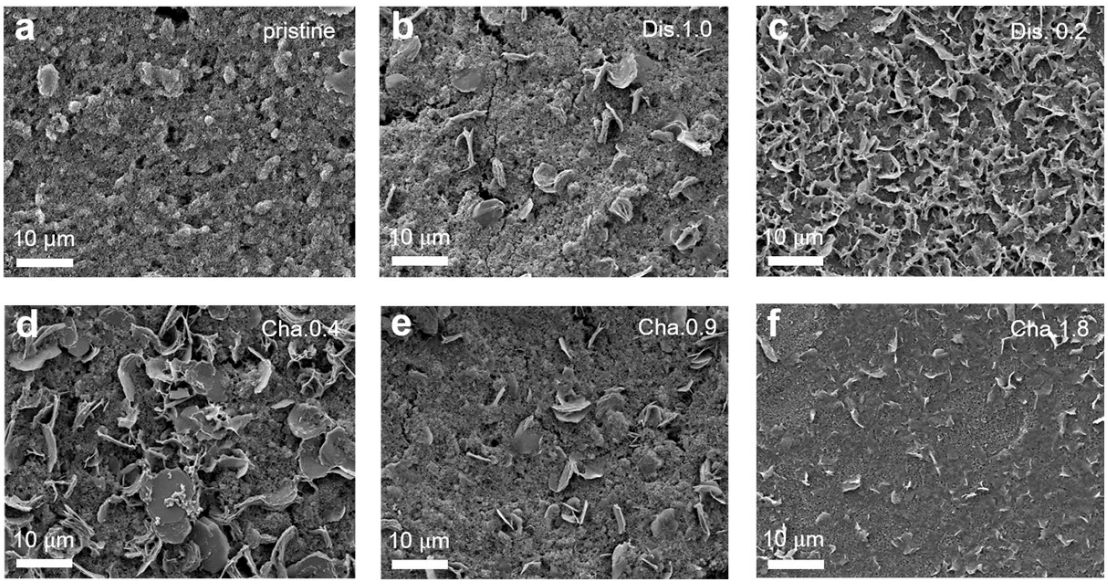

Fig. S15 SEM images of the morphological evolution of the FCVO in different charge/discharge states.

Ex-situ SEM was employed to further visually observe the charging/discharging process. As shown in Fig. S15, the pristine morphology of FCVO is flat without any visible nanosheet. While there are a large number of nanosheets gradually emerging the figure during the discharging to 0.2 V. And these nanosheets disappear again in the period of charging to 1.8 V, further indicating the good reversibility of corresponding electrochemical reactions.[S15]

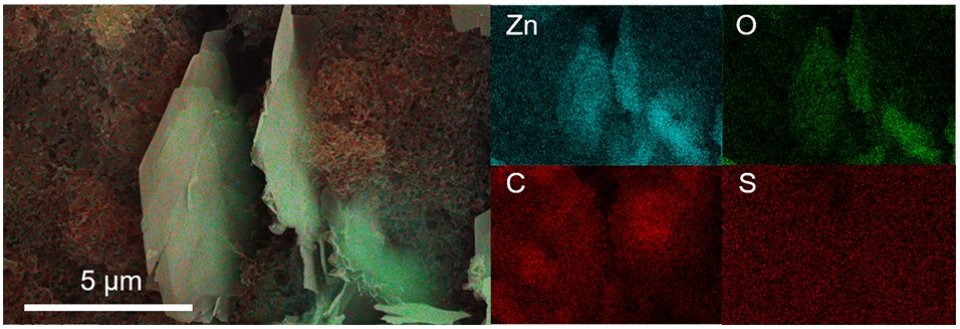

Fig. S16 SEM image and corresponding EDX elemental mapping of the FCVO cathode fully discharged to 0.2 V.

The EDS element mapping analysis of the nanosheets further illustrates that the composition of the nanosheets is $Zn_x(OTf)_y(OH)_{2x-y}\cdot nH_2O$, due to the obviously uniform distribution of Zn, O, S and C elements.

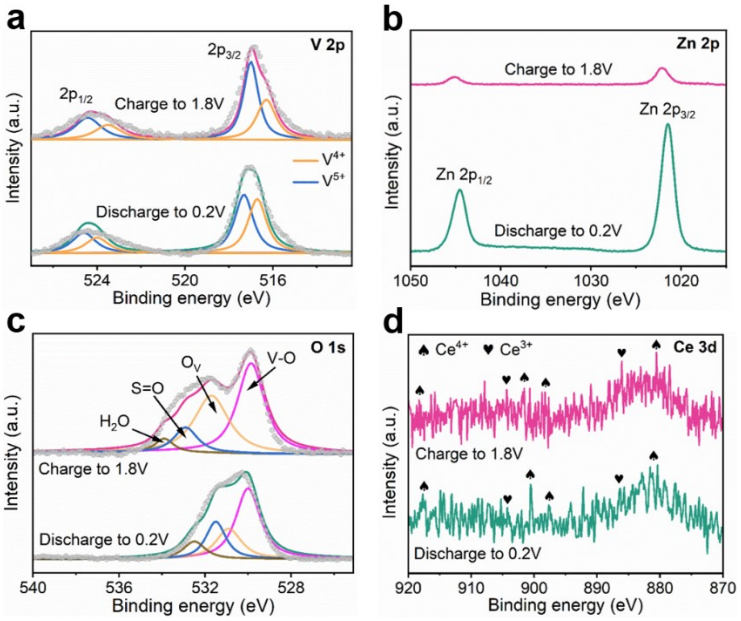

Fig. S17 XPS at different states for (a) V 2p; (b) Zn 2p; (c) O 1s; (d) Ce 3d region.

The *ex-situ* XPS was conducted to further investigate the structural changes of FCVO in different discharging and charging states. As shown in Fig. S17a, the peak of V^{5+} is obvious higher than that of V^{4+} when the FCVO is charged to 1.8 V. While the FCVO is discharged to 0.2 V, the peak of V^{4+} become larger, indicating some high valence V^{5+} has been reduced to V^{4+}.[S5] Moreover, there are two obvious peaks corresponding to Zn $2p_{1/2}$ and Zn $2p_{2/3}$, and the peaks almost disappear when charged to 1.8 V (Fig. S17b), which indicates that the Zn^{2+} intercalation is highly reversible in the FCVO. Compared with O_{1s} spectrum in 1.8V, the characteristic peaks of S=O and H_2O are obviously increasing in the fully discharged state (Fig. S17c), which was revealing the formation of $Zn_x(OTf)_y(OH)_{2x-y}$.[S16] In addition, Ce was basically unchanged at the fully charge and discharge states, indicating the good stability of Ce valance state in FCVO (Figure. S17d).

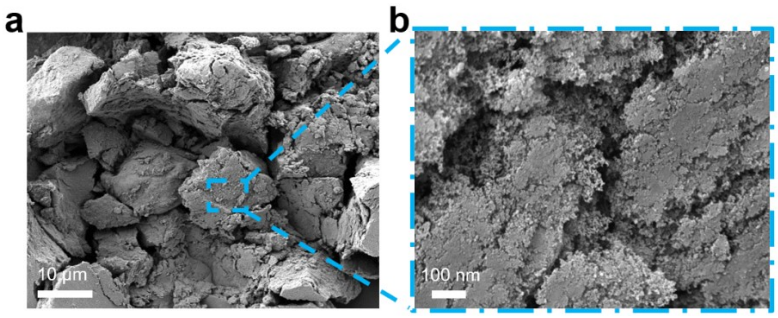

Fig. S18 SEM images of printed FCVO/CB microelectrode with different magnifications.

Table S2 Fitting results of R_s and R_{ct} of the EIS in Figure 3a.

Sample	R_s (Ω)	R_{ct} (Ω)
FCVO/CB	19.6	496.2
FCVO/CB/CNT	10.1	243.7

Note: R_s is the series resistance of the electrochemical system; R_{ct} is the charge-transfer resistance.

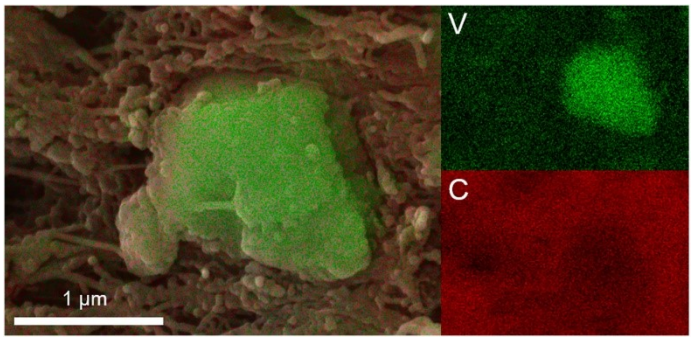

Fig. S19 SEM image and corresponding EDX elemental mapping of FCVO/CB/CNT microelectrode.

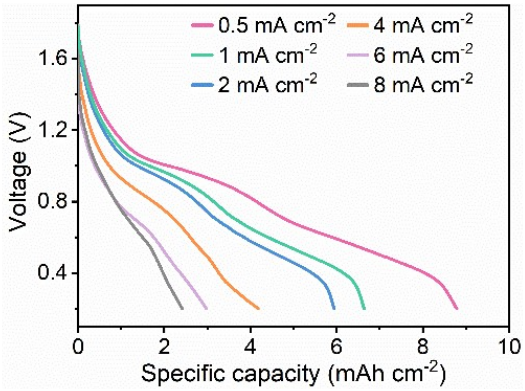

Fig. S20 GCD profiles of FCVO/CB at various current densities.

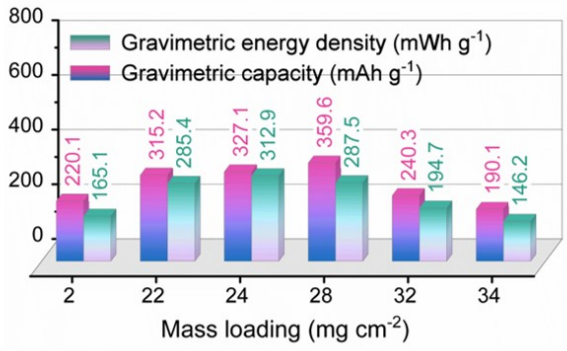

Fig. S21 The gravimetric capacity and energy density of ZIMBs with different materials loading.

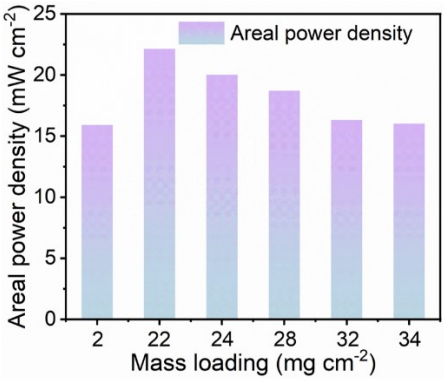

Fig. S22 The areal power density of ZIMBs with different materials loading.

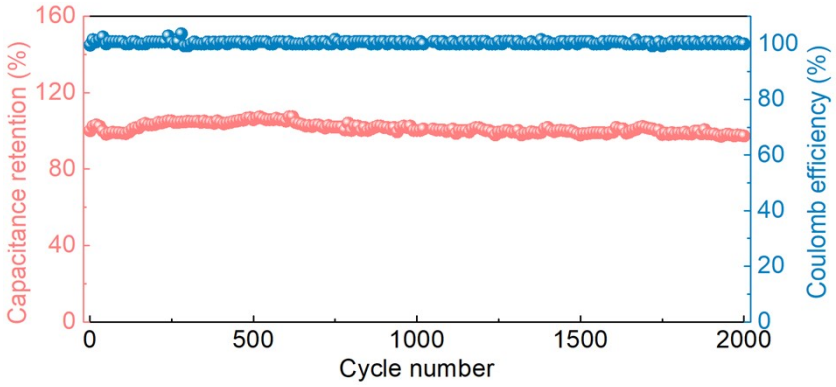

Fig. S23 Long-term cycling stability of the ZIMB at 2 mA cm^{-2}.

Reference

S1 Y. Chen, B. Zhao, Y. Yuan and A. Cao, *Adv. Energy Mater.*, 2022, **12**, 2201834.

S2 P. Zhang, Y. Li, G. Wang, F. Wang, S. Yang, F. Zhu, X. Zhuang, O. Schmidt and X. Feng, *Adv. Mater.*, 2019, **31**, 1806005.

S3 Y. Cui, Y. Xue, R. Zhang, J. Zhang, X. a. Li and X. Zhu, *J. Mater. Chem. A*, 2019, **7**, 21911-21917.

S4 J. Zhang, H. Zhang, M. Liu, Q. Xu, H. Jiang and C. Li, *Chem. Eng. Sci.*, 2020, **227**, 115915.

S5 J. Cao, D. Zhang, Y. Yue, X. Wang, T. Pakornchote, T. Bovornratanaraks, X. Zhang, Z.-S. Wu and J. Qin, *Nano Energy*, 2021, **84**, 105876.

S6 Y. Yang, Y. Tang, S. Liang, Z. Wu, G. Fang, X. Cao, C. Wang, T. Lin, A. Pan and J. Zhou, *Nano Energy*, 2019, **61**, 617-625.

S7 J. Li, K. McColl, X. Lu, S. Sathasivam, H. Dong, L. Kang, Z. Li, S. Zhao, A. G. Kafizas, R. Wang, D. J. L. Brett, P. R. Shearing, F. Corà, G. He, C. J. Carmalt and I. P. Parkin, *Adv. Energy Mater.*, 2020, **10**, 2000058.

S8 F. Ming, H. Liang, Y. Lei, S. Kandambeth, M. Eddaoudi and H. N. Alshareef, *ACS Energy Lett.*, 2018, **3**, 2602-2609.

S9 S. Li, X. Wei, C. Wu, B. Zhang, S. Wu and Z. Lin, *ACS Appl. Energy Mater.*, 2021, **4**, 4208-4216.

S10 Z. Qi, T. Xiong, T. Chen, W. Shi, M. Zhang, Z. W. J. Ang, H. Fan, H. Xiao, W. S. V. Lee and J. Xue, *J. Alloys Compd.*, 2021, **870**, 159403.

S11 Z. Wang, P. Liang, R. Zhang, Z. Liu, W. Li, Z. Pan, H. Yang, X. Shen and J. Wang, *Appl. Surf. Sci.*, 2021, **562**, 150196.

S12 L. Wang, K.-W. Huang, J. Chen and J. Zheng, *Science Advances*, 2019, **5**, eaax4279.

S13 Y. Zhang, F. Wan, S. Huang, S. Wang, Z. Niu and J. Chen, *Nat. Commun.*, 2020, **11**, 2199.

S14 C. Xia, J. Guo, P. Li, X. Zhang and H. N. Alshareef, *Angew. Chem. In.t Ed.*, 2018, **57**, 3943-3948.

S15 S. Li, X. Wei, C. Wu, B. Zhang, S. Wu and Z. Lin, *ACS Appl. Energy Mater.*, 2021, **4**, 4208-4216.

S16 W. Leng, X. Liu and Y. Gong, *Chem. Eng. J.*, 2022, **431**, 134034.